An Airborne Sonar System for Underwater Remote Sensing and Imaging

AIDAN FITZPATRICK, (Graduate Student Member, IEEE), **AJAY SINGHVI**, (Member, IEEE), **AND AMIN ARBABIAN**, (Senior Member, IEEE)

Department of Electrical Engineering, Stanford University, Stanford, CA 94305, USA

Corresponding author: Aidan Fitzpatrick (ajfitz@stanford.edu)

ABSTRACT High-resolution imaging and mapping of the ocean and its floor has been limited to less than 5% of the global waters due to technological barriers. Whereas sonar is the primary contributor to existing underwater imagery, the water-based system is limited in spatial coverage due to its low imaging throughput. On the other hand, aerial synthetic aperture radar systems have provided high-resolution imaging of the entire earth's landscapes but are incapable of deep penetration into water. In this work, we present a proof-of-concept system which bridges the gap between electromagnetic imaging in air and sonar imaging in water through the laser-induced photoacoustic effect and high-sensitivity airborne ultrasonic detection. Here, we use air-coupled capacitive micromachined ultrasonic transducers (CMUTs) which is a critical differentiator from previous works and has enabled the acquisition of an underwater image from a fully airborne acoustic imaging system – a task that has yet to be accomplished in the literature. With the entire imaging system located on an airborne platform, there is much promise for the scalability of our system to one which could perform high-throughput imaging of underwater in large-scale deployment. Non-contact acoustic-based imaging modalities are also of much interest to the medical imaging and non-destructive testing communities. Incorporating air-coupled transducers, for example CMUTs, or other resonant sensors in these applications could be aided by the analysis presented throughout this work.

INDEX TERMS Capacitive micromachined ultrasonic transducer, CMUT, laser Doppler vibrometer, laser ultrasound, non-destructive testing, photoacoustic, sonar, ultrasound, underwater imaging.

I. INTRODUCTION

Sensing and imaging of underwater is an extensive field with applications including biological survey [1], bathymetry [2], wreckage searching [3], defense surveillance [4], among others. To date, sensing in seawater is performed with sonar systems which use ultrasound to obtain high-resolution subsurface images. Sonar systems are typically hull-mounted or towed by ships that traverse an area of interest [5]. With this means of operation, imaging throughput is low – leading to costly and time-consuming efforts when covering large areas. In addition, some applications of underwater imaging may prohibit safe navigation of an in-water sonar system. A more versatile, non-contact or airborne imaging system that is

mounted on a moving platform could permit high-throughput sensing of underwater environments.

Sonar is the state-of-the-art underwater sensing technology due to the high-resolution and long-range capabilities offered by short acoustic wavelengths and low attenuation in water [6]. Despite desirable in-water propagation, ultrasound does not transmit well through the air-water interface – prohibiting the use of a traditional sonar system on an airborne platform.

Prevailing free-space sensing technologies include radar and optical imaging. Due to the high dielectric and conductive losses in seawater, radio-frequency (RF) and microwave energy used for radar imaging cannot penetrate to large depths [7]–[9]. Likewise, optical energy is highly absorbed by water at most wavelengths [10]. Even wavelengths in the visible spectrum that can penetrate deeper into clear water suffer from significant scattering in turbid seawater as a result of their short wavelengths [11], [12]. With radar, optical,

and sonar imaging all lacking the ability to perform airborne imaging of underwater, a novel system must be developed to break through this technological barrier.

To maintain the advantages of underwater acoustic propagation, recent works explore the prospect of a non-contact acoustic source generated through a laser interaction with the surface of water [13]–[16]. While this transmit mechanism shows much promise, these systems rely on detection of echoed acoustic waves through a second laser performing surface vibrometry. As the echoed waves impinge on the surface of water, small displacements can be measured as an optical frequency shift by a laser Doppler vibrometer (LDV) [14]–[16]. The use of an LDV comes with many challenges, however, and has limited the practicality and thus deployment of these systems. Section II provides more insight into the shortcomings of the above-mentioned imaging techniques for this application.

Contributions: To address the gap for high-throughput, scalable airborne imaging of underwater, we propose a system (see Fig. 1) which excites an underwater acoustic source using an airborne laser and detects the acoustic echoes at the airborne platform with collocated high-sensitivity capacitive micromachined ultrasonic transducers (CMUTs) [17]. Since the CMUTs are micro-electromechanical (MEMS) devices, they can easily interface with circuits fabricated on silicon and can be integrated into large arrays [18]. While a large physical array of CMUTs is not in the scope of this work, mechanical scanning of a single CMUT device with coherent detection allows sufficient spatial sampling of the acoustic echoes needed for proof-of-concept image reconstruction [19]. Our proposed CMUT detection technique requires a considerably different system design approach but offers higher sensitivity than the LDV-based methods while also offering potential to scale to large sensor arrays.

Within, we analyze an acoustic interference phenomenon that occurs after laser interaction with the surface of water in order to enable low frequency, narrowband acoustic waves that can be efficiently captured by airborne CMUTs. The presented analysis and design is critical for selecting proper system design parameters such as the laser wavelength and acoustic frequency. We adapt an image reconstruction algorithm for functionality in bistatic layered imaging scenarios, and we demonstrate – for the first time – imaging an underwater environment using a fully airborne system that capitalizes on advantageous underwater acoustic propagation.

The remainder of this paper is organized as follows: Section II discusses the shortcomings of existing technologies and emerging techniques for high-throughput imaging of underwater. Section III provides an overview of our system and introduces the approach for acoustic generation and detection. Section IV analyzes the acoustic interference phenomenon to derive a framework for optimizing key design parameters; the presented theory is experimentally validated to confirm the translation to practical implementation. Section V details the experimental setup as well as the signal processing and image reconstruction algorithm before

presenting the proof-of-concept end-to-end imaging results. Finally, Section VI summarizes the key contributions of this work and proposes future work that will further advance the robustness of our system.

II. RELATED WORKS
In this section, we highlight the shortcomings of conventional imaging technologies (i.e. sonar, radar, and lidar) as well as of surface vibrometry – an emerging approach in application to high-throughput, airborne imaging of underwater.

A. SONAR
As we have previously described, sonar is a fitting in-water sensing system primarily by virtue of its low attenuation in water and thus long-range imaging capability. For this reason, sonar is also attractive for our airborne system which aims to scale to imaging significant depths in water. Unfortunately, sound waves do not transmit well through the air-water interface as a result of a large acoustic impedance mismatch between the two media. The transmission loss (TL) of acoustic waves through the air-water interface can be calculated as:

$$TL = -20 \log_{10} \left(1 - \left| \frac{Z_a - Z_w}{Z_a + Z_w} \right| \right) = 65 \, dB. \quad (1)$$

where Z_a is the acoustic impedance of air ($\sim$420 *Rayl*) and Z_w is the acoustic impedance of water ($\sim 1.5 \times 10^6$ *Rayl*) [20]. The significance of this transmission loss is that the amplitude of the acoustic pressure wave diminishes by 65 *dB* as it propagates through the interface. Commonly, the amplitude of the acoustic pressure wave is quantified using a measure known as sound pressure level (SPL) which is defined as:

$$SPL = 20 \log_{10} \left(\frac{p}{p_{ref}} \right), \quad (2)$$

where p is the root mean square (RMS) pressure and p_{ref} is the reference pressure that we will take to be 1 μPa – the typical reference for underwater sound [21].

If we were to attempt using a sonar system on an airborne platform, the acoustic wave would encounter approximately 130 *dB* loss to the SPL: 65 *dB* as the sound waves transmit into the water and again another 65 *dB* as the echoed waves return into air for detection. This two-way interface loss would be problematic even with the most sensitive of receivers.

B. RADAR
Radio wave propagation in water is largely constrained as a result of high absorption and thus limited penetration depth. Extremely low frequency (ELF) and very low frequency (VLF) radio waves have been historically used for communication to submarines with frequencies in the range of 3 *Hz* − 3 *kHz* for ELF or 3 *kHz* − 30 *kHz* for VLF; at these frequencies penetration depths of 10 *m* for VLF or as much as 100 *m* for ELF can be achieved [22]. The wavelengths at these frequencies, however, are on the order of tens of kilometers requiring massive antennas with poor radiation efficiencies [23]. Besides antenna restrictions, the large wavelengths and

limited available bandwidth at these frequencies will prohibit imaging with acceptable resolution. To design a system with reasonable antenna sizes and sub-meter scale resolution, *GHz* frequencies must be used where penetration depth in water is on the order of millimeters [8], [9].

C. LIDAR

Out of the conventional active imaging approaches discussed here, lidar proves to be the most applicable for underwater imaging from an airborne platform. In the visible spectrum, specifically with blue-green laser light, optical absorption is as low as 0.5 *dB/m* [10] – permitting high penetration depths in pure water. However, where lidar begins to fail is in practical ocean environments where particulate matter of considerable size relative to the short optical wavelengths is suspended in the water.

Babin *et al.* [12] studied scattering of light at 555 *nm* as a function of suspended particulate matter across several coastal regions and bodies of water; this study is relevant here due to the optical wavelength falling near the range of minimum absorption. They found that the scattering coefficient fell mostly within the range of 0.1 – 10 m^{-1} and as high as 30 m^{-1} in coastal waters with extreme turbidity [12]. Combining the effects of both optical absorption and optical scattering, attenuation could range from 0.5 *dB/m* in clear water to 45 *dB/m* in turbid water or even greater than 100 *dB/m* in extreme turbidity conditions. Despite ongoing research for airborne lidar imaging of underwater [24]–[30], the limited imaging depth and lack of robustness of these lidar systems to turbidity – especially in coastal waters – warrants exploration of alternative approaches that exploit favorable underwater acoustic propagation.

D. SURFACE VIBROMETRY

Many works have studied the generation of an underwater acoustic source through a non-contact manner for applications including communication and sensing [13]–[16], [31]. Typically, these solutions rely on a laser interaction with the surface of water; the underlying physics of this interaction are further described in Section III. As we previously explained, the sensing systems employing this acoustic source mechanism detect the echoed acoustic waves through surface vibrometry using an LDV. While these systems are able to take advantage of underwater acoustic propagation, the LDV detection faces many challenges in a practical imaging system.

The use of LDVs is a common approach for non-contact detection of acoustic signals in many applications [32]. In applications where spatial information is not critical, a single point LDV can be used to detect acoustic pressure waves with high sensitivities in the ballpark of 50 $mPa/\sqrt{Hz}$ or equivalently in SPL: 94 *dB re.* $\mu Pa/\sqrt{Hz}$ [33]. It is notable that the high sensitivities achieved by LDVs in the literature are made possible through strong optical reflections from the detection surface; sensitivity would be diminished for the minimally reflective water surface [14]–[16], [31].

Antonelli *et al.* measured a minimum detectable signal of 120 *dB re.* $\mu Pa/\sqrt{Hz}$ using a commercial LDV on the surface of water [14].

On the other hand, if it is desired to capture and reconstruct an image, the LDV can be mechanically scanned across the medium [33]–[37]. The stipulation here, however, is that the measurement conditions remain static in order to have robust synchronization of phases [38]. With a moving airborne platform and dynamic water surface, the requirement for static measurement conditions is unlikely to be sustained for the desired application. To overcome this limitation, there has been much effort on the development of multi-point or multi-beam LDVs which probe the detection surface simultaneously in several locations [38]–[41]. To date, these multi-point LDVs have been limited to a small number of channels and prove to be expensive to scale. The limited number of channels currently feasible for multi-point LDVs cannot provide sufficient spatial sampling of the underwater acoustic signals for large-scale imaging.

In the next section, we propose a system that enables detection of acoustic waves in air with highly sensitive air-coupled transducers that can be easily scaled to provide the array processing capability that is currently limiting the LDV-based approaches. While our system also utilizes a laser interaction with the surface of water for acoustic source generation, we must carefully design the laser excitation such that it is applicable for airborne ultrasonic detection.

III. OVERVIEW OF PROPOSED SYSTEM

A. SYSTEM CONCEPT

Photoacoustic imaging is an emerging modality in the medical community that has made much progress over the past decades due to its good optical contrast and high-resolution [42]. In our sensing application, we employ the photoacoustic effect not for its contrast or resolution but instead to capitalize on both the favorable airborne propagation of optical energy and the favorable underwater propagation of acoustic energy. Herein, we introduce an airborne sonar system concept for non-contact underwater imaging that utilizes the photoacoustic effect.

1) PROPOSED SYSTEM

A schematic of our proposed system is shown in Fig. 1. A laser that is intensity modulated at the desired acoustic frequency is used to excite acoustic waves via the photoacoustic effect at the water surface; the generated acoustic waves propagate underwater similarly to conventional sonar; the acoustic waves reflect off of objects in the water and in some part transmit through the air-water interface; high-sensitivity CMUTs capture the acoustic echoes in air; post-processing of received signals is performed to generate an image of the underwater targets.

By exploiting laser-induced acoustics, we bypass the penetration depth limitation of an all-optical or all-RF system. Likewise, we prevent the transmission loss into water
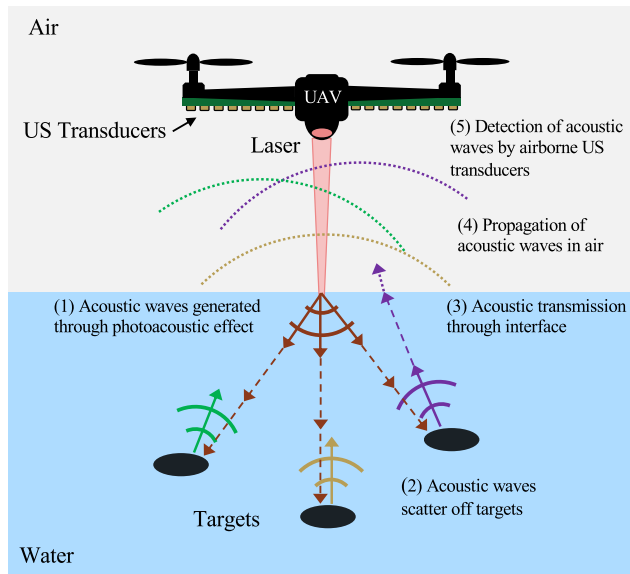
FIGURE 1. Schematic of proposed airborne sonar system with the exciting laser and receiving ultrasound (US) transducers both on-board an airborne platform which here is depicted as an Unmanned Aerial Vehicle (UAV).

that would be encountered for a purely ultrasonic system. Our hybrid optical-acoustic approach can operate at a standoff – though not without challenges.

2) SIGNAL STRENGTH CHALLENGE

Ultrasonic imaging with CMUTs in air is a technically challenging problem that imposes a unique design space for this new class of airborne imaging systems. Whereas the photoacoustic excitation of the acoustic source in water bypasses the 65 dB transmission loss on the source side, the acoustic echoes still encounter a one-way 65 dB loss as they propagate from the water into air. This one-way transmission loss is still substantial and poses signal-to-noise (SNR) challenges on the received signals. To maintain high-sensitivity ultrasonic detection despite the large acoustic impedance mismatch, the CMUTs are designed to be narrowband, resonant sensors with high quality factors [19]. In contrast to the wideband LDV-based detection, the acoustic signals are now required to have multiple cycles at the CMUTs' resonance frequency as depicted in Fig. 2 – demanding a different approach for laser excitation of the underwater acoustic source.

B. LASER ACOUSTIC EXCITATION

There are effectively three mechanisms for generating underwater pressure waves using a laser: dielectric breakdown, vaporization, and thermoelastic expansion [43]–[46]. Each of these mechanisms has their own advantages and disadvantages that are application dependent.

1) DIELECTRIC BREAKDOWN

Dielectric breakdown of water occurs when a laser of extremely high intensity, on the order of 100 MW/cm^2,

is incident on the surface [43], [47], [48]. The strong electromagnetic fields in the water cause a plasma formation that results in high-efficiency absorption of incident optical energy. The plasma rapidly expands as its temperature rises dramatically and detonates shortly after formation [43], [47]. This results in a detonation wave that propagates into the water with extremely high SPL [49].

Despite the high pressure levels, this mechanism is less than ideal for an imaging system. Firstly, this degree of intensity often requires tight optical focusing on the surface of water which is difficult to achieve with a dynamic ocean surface [13]. In addition, the detonation wave has a stochastic phase and travels arbitrarily faster than the speed of sound which complicates coherent image reconstruction [43]. Finally, in application to our system specifically, the pressure wave is rather broadband and could not be efficiently captured by our resonant, narrowband CMUTs.

2) VAPORIZATION

Vaporization, or the phase change of the water to vapor, requires high energy density of the incident laser – greater than 2.3 kJ/cm^3 [13]. When vapor escapes from the water surface, a recoil force is caused as momentum is transferred [43], [45]. This force results in a broadband pressure wave that is still high in SPL though lesser than that of the detonation wave [44].

The vaporization mechanism has been used in laser-induced acoustic communication to underwater receivers by relying on on-off keying techniques [15], [50]. However, the pressure waves generated through the vaporization mechanism are not apt for an imaging system. Whereas the pressure waves now travel at the speed of sound in water, they remain stochastic in phase, are broadband, and result from a nonlinear process that is complicated to model and handle analytically [43].

3) PHOTOACOUSTIC EFFECT

Thermoelastic expansion, which when induced by a laser is often referred to as the photoacoustic effect, is the process of volumetric expansion of the water upon heating [46]. This volumetric expansion results in a propagating pressure wave in the water that is of lesser SPL than can be generated by the other two mechanisms [43]–[46].

The advantage of photoacoustic excitation of the underwater acoustic source is that it is a linear process – meaning that the intensity modulation of the incident laser directly controls the amplitude and phase of the pressure wave [46], [51], [52]. The linear nature of the photoacoustic effect thus allows us to excite resonant acoustic waves at the desired acoustic frequency [43], [53] while enabling coherent processing for image reconstruction. When exciting acoustic waves at the surface of water, the photoacoustic conversion efficiency is no longer optimized with highest optical absorption – as it is in conventional medical photoacoustic imaging [42], [46]. Section III presents in-depth analysis of the photoacoustic effect at the surface of water, which articulates the need for

careful design of key system parameters in such non-contact, narrowband imaging systems.

C. AIRBORNE ULTRASOUND DETECTION

In medical ultrasound [54] and photoacoustic imaging [55], a coupling medium is required to improve the impedance matching of the transducer to the skin and tissue. Without the coupling medium, the existence of air gaps prohibits acoustic detection by the transducer elements not in perfect contact. As discussed earlier, this is due to the sizable impedance mismatch between air and tissue and is analogous to why our system is SNR-constrained. The impedance mismatch and the corresponding transmission loss of the acoustic waves from water to air is inherent to our airborne system and must be compensated for with high receiver sensitivity.

Air-Coupled CMUTs: To compensate for the large 65 *dB* loss, we utilize air-coupled CMUTs. CMUTs are proving to be a superior solution to piezoelectric transducers for the problem of efficiently receiving sound waves in air [56], [57]. These transducers are simple capacitors with a thin plate that is set into vibration by impinging ultrasound waves [58]. The displacement of the thin plate results in a change in capacitance that is in turn detected by interfacing the CMUT with appropriate electronic circuitry. The high efficiency of CMUTs is due to the large DC electric field across the electrodes (plate and substrate) which permits good signal transduction and the fact that the thin vibrating plates have a mechanical impedance that is well-matched to air [56].

The CMUT used herein operates at a center frequency of 71 *kHz* and has been previously reported in prior works [19], [59], [60]. The CMUT was designed to operate at a low acoustic frequency to limit the attenuation in air: approximately 165 *dB/m* at 1 *MHz*, while only 3 *dB/m* at 100 *kHz* [61]. It is clear that operating at acoustic frequencies in the *MHz*-range would limit receiver standoff to a few centimeters; however, at lower acoustic frequencies, meter standoffs are possible with reasonable attenuation while still achieving *cm*-scale resolution [19].

The detection sensitivity of the 71 *kHz* CMUT is 5.5 $\mu Pa/\sqrt{Hz}$ or in SPL: 14.8 *dB re.* $\mu Pa/\sqrt{Hz}$. To compare this sensitivity to the LDV-based detection methods, we can add back the 65 *dB* in transmission loss across the air-water interface to have a fair comparison. Doing so, we note detection sensitivity on the order of 80 *dB re.* $\mu Pa/\sqrt{Hz}$ for acoustic waves incident on the water surface. This is considerably more sensitive than LDV detection – especially that reported by Antonelli *et al.* of 120 *dB re.* $\mu Pa/\sqrt{Hz}$. In addition, even more sensitive air-coupled CMUTs have shown greater than 13 *dB* better sensitivity than those used in this work [17].

This level of sensitivity, however, comes with a sensitivity-bandwidth trade-off in order to limit the noise contribution. The device has a fractional bandwidth of 3.5%, or equivalently a high quality factor (Q) of 28.5. This limited bandwidth requires multiple impinging acoustic cycles at the CMUT's resonance frequency in order to ring up to full
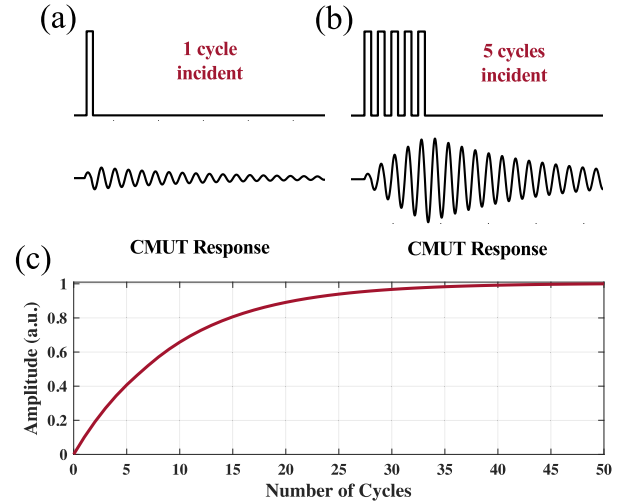

FIGURE 2. (a), (b) Top: Number of acoustic cycles incident on CMUT; Bottom: Corresponding CMUT response to the above number of cycles, (c) Maximum amplitude of CMUT response versus the number of incident acoustic cycles.

sensitivity as illustrated in Fig. 2. For our SNR-constrained system, the additional sensitivity gained through multiple cycles is critical.

The multi-cycle, narrowband source requirement is in contrast to other sensing modalities which aim to use either short, delta-like pulses or wideband frequency-domain signals for enhanced imaging resolution [62]. Despite the narrowband CMUTs, with a sufficiently large aperture our system achieves reasonable imaging resolution on the order of the acoustic wavelength [19], which is approximately 2 *cm* in water for a 71 *kHz* acoustic wave.

Whereas the CMUTs are critical for high-sensitivity detection and array processing capability, the low frequency, narrowband source requirement imposes new challenges that are not common in traditional imaging systems and thus has required us to perform thorough analysis and novel design.

IV. SYSTEM ANALYSIS & DESIGN

In this section, we analyze the photoacoustic excitation of acoustic waves at the surface of water. As will be described, there is an acoustic interference phenomenon that presents a fundamental challenge and imposes strict design constraints particularly on the laser wavelength. By analyzing the laser-water interaction, we discuss heuristics for selecting the laser wavelength and acoustic frequency. We also investigate the impact of the laser beam radius on the propagation of the underwater acoustic waves.

When the optical energy is absorbed at the surface of water, a propagating pressure wave is generated via the photoacoustic effect and is governed by the wave equation [42]:

$$\left(\nabla^2 - \frac{1}{v_s^2}\frac{\partial^2}{\partial t^2}\right)p(\mathbf{r}, t) = -\frac{\beta}{C_p}\frac{\partial h(\mathbf{r}, t)}{\partial t}, \tag{3}$$

where v_s is the speed of sound, $p(\mathbf{r}, t)$ is the acoustic pressure at position $\mathbf{r}$ and time t, β and C_p are the thermal
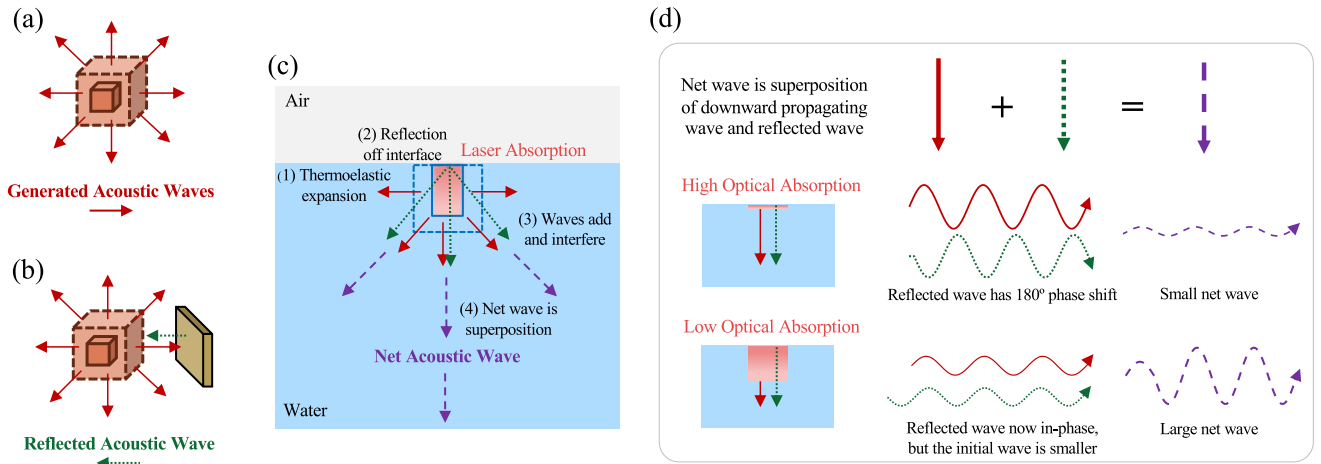
FIGURE 3. (a) Photoacoustic-generated waves due to thermal volumetric expansion, (b) Reflected acoustic wave off a mechanical discontinuity, (c) Net acoustic wave which is the coherent sum of the generated and reflected acoustic waves, (d) Role of optical absorption in the superposition of the reflected wave with the downward propagating wave.

expansion coefficient and specific heat capacity of the absorbing medium, and $h(\mathbf{r}, t)$ is the heating function defined as the power deposited per unit volume by the optical excitation. The heating function encapsulates all aspects of the system design as the remainder of the variables are medium-dependent.

Acoustic Wave Reflections: It is important to analyze the wave equation in order to optimally design our heating function (or the incident optical energy) and maximize the SPL of the propagating pressure wave and thus SNR at the receivers. Before doing so, it is useful to qualitatively consider the photoacoustic interaction to gain intuition into the results of a more rigorous analysis.

As shown in Fig. 3(a)-(c), an optical absorber expands and generates outward propagating pressure waves when there is no impeding boundary; however, when a medium of high contrast in acoustic impedance is present, the pressure wave is reflected due to the mechanical discontinuity. In the context of laser absorption at the water surface, the air-water interface is that mechanical discontinuity which results in a reflected wave that will superimpose with the downward propagating wave.

The impact of the reflected wave needs to be carefully considered when selecting the laser wavelength, which dictates the degree of optical absorption. As depicted in Fig. 3(d): if the laser is strongly absorbed in a depth much smaller than the acoustic wavelength, the reflected wave will have a strong destructive interference effect; however, if the laser has lesser absorption, the reflected wave can align in-phase with the downward propagating wave culminating in a larger net wave. In Fig. 3(d), it is important to note that a laser which has lower optical absorption has a less efficient conversion of optical energy to acoustic energy [42], [46] resulting in the initial waves having smaller amplitude. That being said, to maximize the SPL of the net wave, there is a trade-off between interference and opto-acoustic conversion efficiency

TABLE 1. Definition of design equation symbols.

Symbol	Definition
P	spectral magnitude of the acoustic pressure
$\mathbf{r}$	position vector (refer to Fig. 13)
ω	angular acoustic frequency
T	optical transmission coefficient
β	thermal expansion coefficient of water
C_p	specific heat capacity of water
H_0	peak laser power
$\tilde{H}(\omega)$	normalized optical modulation function
k	acoustic wavenumber in water
μ	optical absorption coefficient of water
θ	angle from interface normal (refer to Fig. 13)
a	laser beam radius

that will result in an optimal degree of optical absorption and thus an optimal laser wavelength.

Whereas Fig. 3 depicts a high-level qualitative analysis, a more rigorous analysis can be performed by solving the photoacoustic wave equation. As will be shown, the derived design equation provides insight into the primary degrees-of-freedom of our system.

A. DESIGN EQUATION
The solution to the wave equation in (3) assuming a Gaussian laser beam is [50], [63]:

$$P(\mathbf{r}, \omega) = \frac{-T\omega\beta}{2C_p} \frac{H_0\tilde{H}(\omega)e^{-jkr}}{r} \frac{\mu k cos\theta}{\mu^2 + k^2 cos^2\theta} e^{-k^2 a^2 sin^2\theta/4},$$

$$(4)$$

where the equation symbols are defined in Table 1. More details for the derivation of (4) can be found in the Appendix.

The time-domain expression of the pressure wave can be computed as the real part of the inverse Fourier Transform of (4); however, since our system exploits narrowband
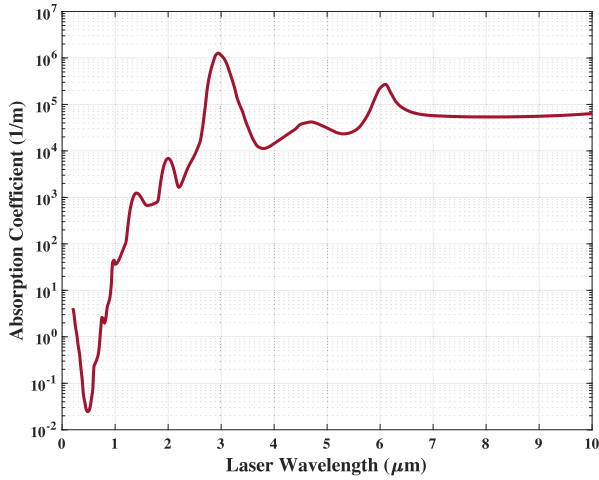
FIGURE 4. Optical absorption coefficient in pure water as a function of the laser wavelength.

FIGURE 5. Comparison of the impact of destructive interference on a 71 *kHz* sinusoidal excitation versus a broadband 50 *ns* pulse excitation.

acoustic waves, the frequency-domain form of the solution is convenient. Whereas in this work we focus on single frequency acoustic signals, (4) could also be solved for wideband optical modulation functions such as conventionally used nanosecond photoacoustic excitations through a Fourier decomposition.

We can determine pertinent system parameters through optimization of the design equation in (4) which shows the controllable parameters as the laser wavelength, laser beam radius, and acoustic frequency while the remainder of the variables are medium-dependent.

B. LASER WAVELENGTH

In conventional photoacoustic imaging, it is typical to choose a laser wavelength that is strongly absorbed to ensure maximum efficiency conversion of optical energy to acoustic energy [42], [46]; the relationship between laser wavelength and optical absorption coefficient in water is depicted in Fig. 4. If this principle is applied here, one may select a 10.6 μm laser wavelength [13] which is commercially available and is highly absorbed by water; this choice of laser would ultimately result in severe destructive interference and appreciable loss in SPL for our excitation. When the optical excitation of acoustic waves occurs at the interface of media with a considerable acoustic impedance mismatch, the analysis below proves to be more insightful for selecting a laser wavelength.

1) OPTIMAL WAVELENGTH

Here, we analyze (4) to determine the optimal laser wavelength for our system. The optimal laser wavelength is that which has the absorption coefficient in water that maximizes the SPL of the net pressure wave, or the superposition of the reflected wave with the downward propagating wave.

For simplicity of this section and since it is desired to maximize the SPL of the wave propagating to the depth of water, we consider (4) where $\theta = 0$ or on the z-axis
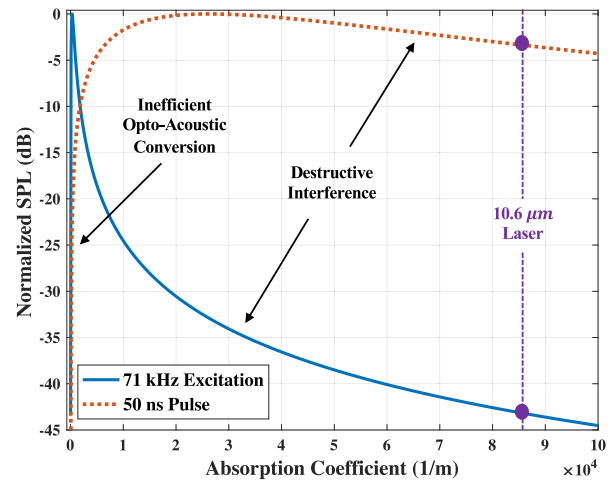
(see Fig. 13):

$$P(z, \omega) = \frac{-T\omega\beta}{2C_p} \frac{H_0\tilde{H}(\omega)e^{-jkz}}{z} \frac{\mu k}{\mu^2 + k^2}. \quad (5)$$

Note that (4) and (5) are expressed in terms of spectral magnitude, but that they can be converted to SPL using (2). The third term of this expression shows that the SPL of the pressure wave has a bandpass structure as a function of the optical absorption coefficient μ. The regions of this term are as follows:

$\mu < k$: Inefficient opto-acoustic conversion
$\mu = k$: Optimal degree of absorption
$\mu > k$: Destructive interference of waves

This term and consequently the SPL of the net pressure wave are optimized when the optical absorption coefficient is equal to the acoustic wavenumber, i.e. $\mu = k$ [63]. Whereas in this work we are focused on single frequency acoustic waves, in the case of wideband laser excitations, the destructive interference effect would still attenuate the low frequency components where $\mu > k$.

In the case of wideband excitations, however, the impact of destructive interference is less detrimental to the system performance. We refer to [13] as an example which uses a 50 *ns* pulse width and a 10.6 μm laser. A 50 *ns* pulse width has a first-null bandwidth of 20 *MHz*. The acoustic wavenumber in water at 20 *MHz* is approximately 80,000 m^{-1} while the optical absorption coefficient at 10.6 μm nears 100,000 m^{-1} as shown in Fig. 4. This means that for the bulk of the frequency content in the 50 *ns* pulse, $\mu > k$ and destructive interference is attenuating the resultant SPL. In this case, however, since the generated acoustic waves are broadband and consist of higher frequencies, the net SPL of the pressure wave is less sensitive to the optical absorption coefficient. This can be seen in Fig. 5 which plots the solution to (5) at the resonance frequency of our CMUTs (i.e. $\omega = 2\pi \cdot 71$ *kHz*) and the integration over the solution to (5) evaluated for the frequency content in a 50 *ns* pulse excitation.
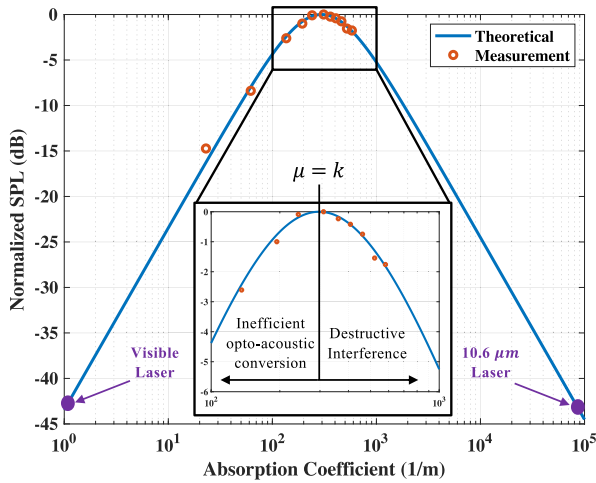
FIGURE 6. Normalized SPL at *z* = 20 *cm* as a function of the optical absorption coefficient for a 71 *kHz* modulated laser with peak power of 500 *W*. Measurement results are scattered over the theoretical curve.

For our 71 *kHz* excitation a steep optimum absorption coefficient exists after which destructive interference largely attenuates the SPL. On the other hand, for the 50 *ns* pulse, the destructive interference does not result in the SPL being as sensitive to the optical absorption coefficient. As a result, the choice of laser in [13], while far from the optimal absorption coefficient, does not impact the SPL considerably. Therefore, while this analysis of the optimal laser wavelength has been noted in other works [50], [63], it becomes critical for applications with CMUT detection where low-frequency, narrowband acoustic waves are used, i.e. where *k* is low.

2) EXPERIMENTAL VALIDATION
In Fig. 6, we again plot (5) at the resonance frequency of our CMUTs but now on a log-scale of the absorption coefficient; this is done for clarity of the representation. In the plot, we compare the analytically predicted SPL to the experimentally measured SPL using a calibrated hydrophone at a $z = 20$ *cm* depth in water. For the experiment, we use a modulated 1070 *nm* multi-modal laser with 500 *W* peak power. Whereas a fixed laser wavelength has a fixed optical absorption coefficient in pure water, we incrementally increase the optical absorption coefficient artificially by adding black ink. For each addition of black ink, the absorption coefficient is determined through an optical transmission measurement similar to that performed in [64]; it is confirmed experimentally that the black ink has negligible impact on the acoustic properties of the water.

Both analytically and experimentally, we see the impact of the reflected wave: as the absorption coefficient increases beyond the optimum of $\mu = k$, the net SPL decreases as a result of destructive interference.

The laser wavelength that results in $\mu = k$ for 71 *kHz* in pure water is 1250 *nm* as read from Fig. 4. For context, if we select a 10.6 *μm* laser based on the principles of conventional photoacoustic imaging or following the work

in [13], we would sacrifice almost 45 *dB* in SPL due to the destructive interference.

C. ACOUSTIC FREQUENCY
While we use a 71 *kHz* CMUT (due to current availability) in the experimental results section of this work, the optimal laser wavelength depends on the acoustic frequency as seen by the relation $\mu = k$. Therefore, in a final system design, optimizing the laser wavelength should not be decoupled from selecting an appropriate acoustic frequency. Instead, one could maximize the SNR of the system by finding the pair of acoustic frequency and laser wavelength that are jointly optimized.

Assuming the bandpass term discussed above can be later maximized through proper selection of laser wavelength, one can see that (4) shows a linear dependence on acoustic frequency ω. This suggests that the SPL of the net pressure wave can be maximized at higher frequencies; however, this equation does not capture propagation effects. To fully optimize over the link budget for SNR at the receiver using acoustic frequency as a design knob, one could use the following relationship:

$$P_{CMUT}(\omega) \propto \omega \frac{\mu k}{\mu^2 + k^2} A_w(d) A_a(h), \qquad (6)$$

where:

$$A_w(d) = 10^{-\alpha_w(\omega)*d/20}, \qquad (7)$$
$$A_a(h) = 10^{-\alpha_a(\omega)*h/20}. \qquad (8)$$

In these expressions, P_{CMUT} is the pressure at the CMUT receiver, d is the round-trip distance traveled in water, h is the receiver height in air, and α_w and α_a are the attenuation in water [65] and air [61] with units *dB/m* as shown in Fig. 7. This neglects frequency dependent scattering off of the targets since this is difficult to know a priori. Nevertheless, over the small range of useful frequencies limited by attenuation, this would likely be frequency insensitive.

The expression in (6) can be used to frame the system design: for a desired receiver height in air and maximum imaging depth, the optimal laser wavelength and acoustic frequency pair that maximizes (6) can be found. For clarity, Fig. 8 depicts an example of this trade-off space by using the relationship of optical absorption coefficient to laser wavelength shown in Fig. 4. It is clear that the optimal system parameters are less impacted by distance travelled in water and are heavily influenced by the acoustic attenuation in air and thus height of the receivers.

Ultimately, when designing a system that utilizes commercially available lasers, one will not have the freedom to choose the optimal laser wavelength with any desired amount of optical power. Instead, it would be valuable to further append (6):

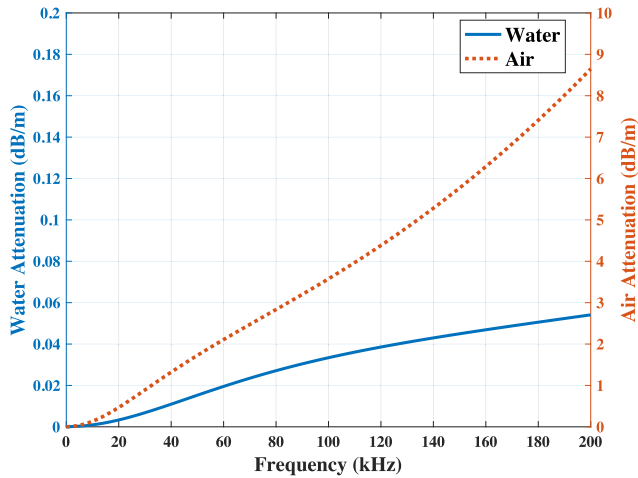$$P_{CMUT}(\omega) \propto \omega \frac{\mu_i k}{\mu_i^2 + k^2} H_i(\omega) A_w(d) A_a(h), \qquad (9)$$

FIGURE 7. Attenuation in water (left) and air (right) up to 200 *kHz* acoustic frequency. The solid line corresponds to water or the left axis and the dashed line to air or the right axis.
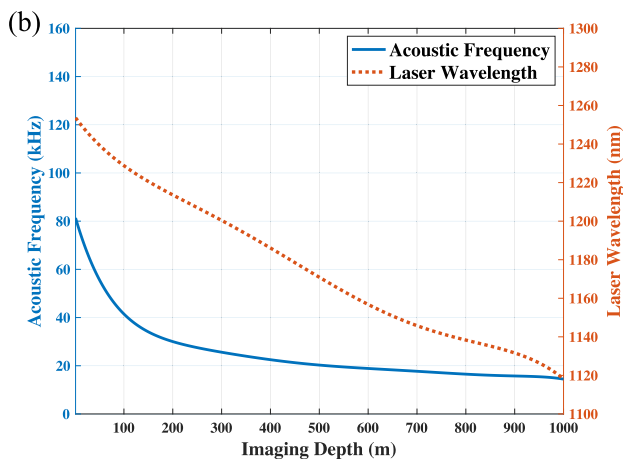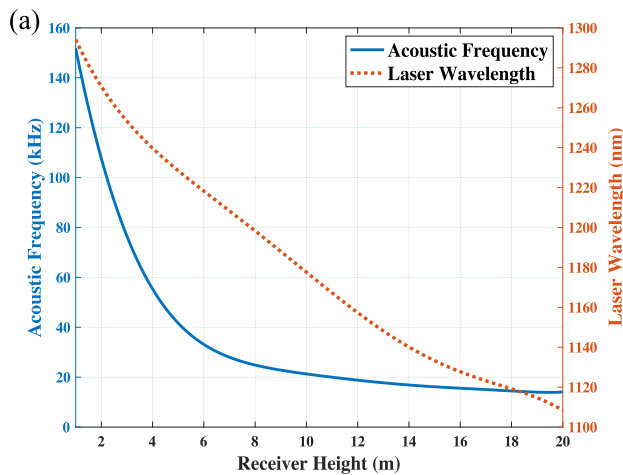

FIGURE 8. Optimum laser wavelength (right) and acoustic frequency (left) as a function of (a) the receiver height in air with *d* = 40 *m* and (b) the imaging depth in water with *h* = 3 *m*. Note the difference in scale for receiver height and imaging depth.

where the subscript i denotes the commercially available options with output power $H_i(\omega)$ and wavelength that corresponds to the optical absorption coefficient μ_i.
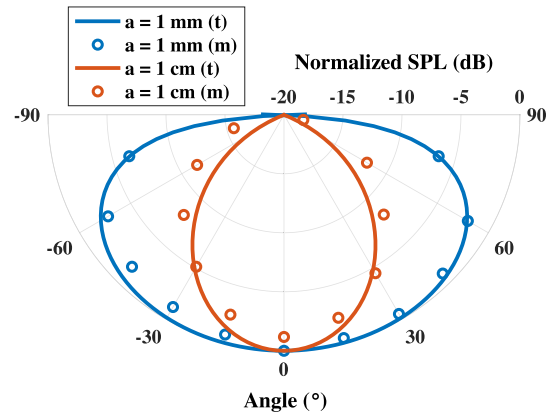

FIGURE 9. Normalized directivity (*dB*) of a 71 *kHz* acoustic source for laser beam radii of 1 *mm* and 1 *cm*. Measurement (m) results are scattered over the corresponding theoretical (t) plots.
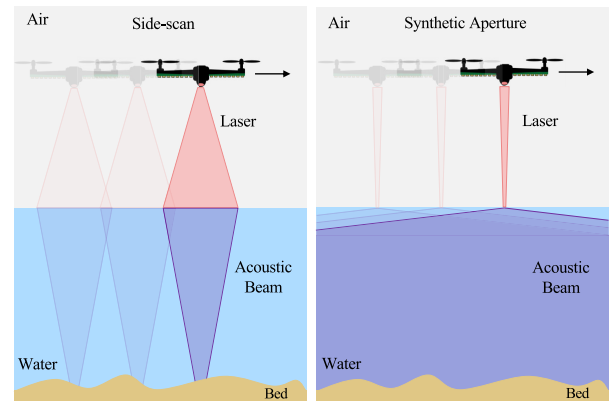

FIGURE 10. Possible imaging modes for our system and their relation to the laser beam radius. *Left:* Side-scan operation. *Right:* Synthetic aperture operation.

Whereas low-power diode lasers are available at nearly any wavelength, Ytterbium-doped lasers near 1064 *nm* and Erbium-doped lasers near 1550 *nm* are some of the most common high-powered lasers with nearby wavelength to the range found in Fig. 8. That being said, one could use (9) to deviate from the optimum laser wavelength while still maximizing SNR when deciding between commercially available lasers.

D. LASER BEAM RADIUS

Here, we discuss the impact of the laser beam radius (a) on the underwater propagating pressure waves. Fig. 9 plots (4) as a function of the angle in water (θ) for two different beam radii: 1 *mm* and 1 *cm*. This is confirmed experimentally with careful alignment of the calibrated hydrophone at a constant distance from the source of $r = 20$ *cm*. These measurements are performed in water with a level of black ink that results in $\mu = k$; it is important to note that the directivity pattern for a given laser beam radius is a function of the absorption coefficient and acoustic frequency.

As seen in the plot, the acoustic directivity, or the focusing of the acoustic energy, increases with larger beam radius;
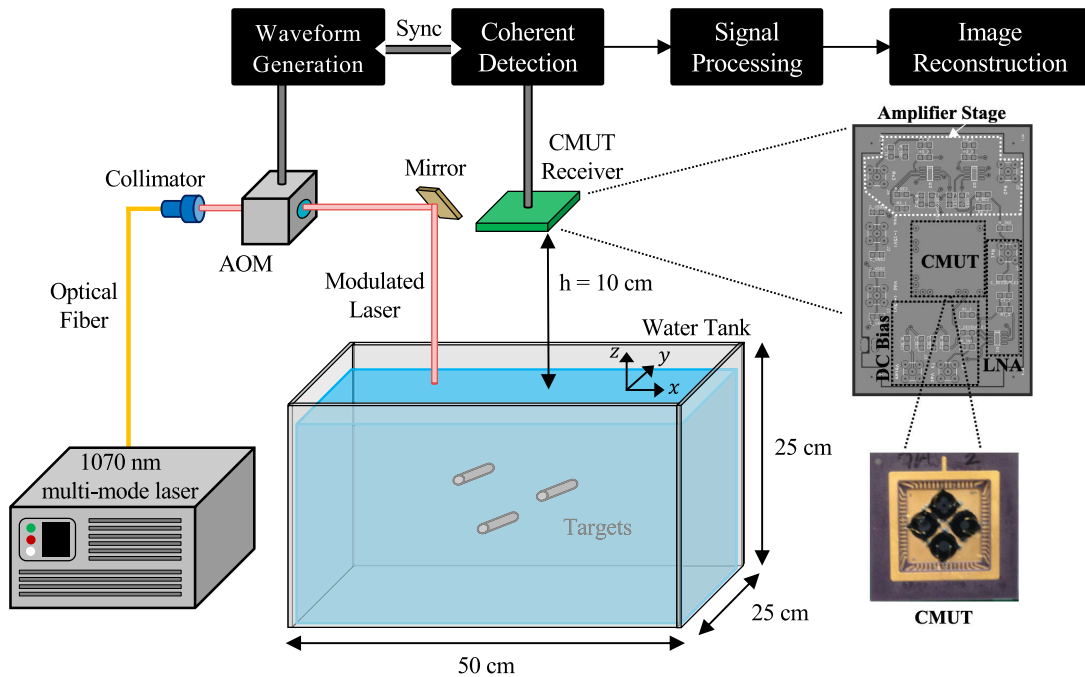
FIGURE 11. The experimental setup used to capture end-to-end airborne imaging of underwater. The coordinate system used for the derivation of the image reconstruction algorithm is noted on the water surface.

however, the SPL at $\theta = 0$ remains constant. The focusing that is observed is a result of the acoustic source having a larger transmitting aperture size. The fact that the SPL is constant at $\theta = 0$ is a surprising result at first glance. In conventional radar, sonar, and lidar, increasing the transmitting aperture size with a constant power results in higher power density that can be captured by a receiver in the direction of the focusing. This results in a trade-off between SNR which can be gained with greater focusing and field-of-view which is reduced with greater focusing in these conventional imaging modalities [6], [23].

For our system, Fig. 9 shows that we can use a smaller beam radius to gain field-of-view without loss to SNR – effectively breaking the above-mentioned trade-off. The trade-off does not hold for our application due to the fact that the pressure generated via the photoacoustic effect is a function of laser intensity and not laser power; therefore, a smaller beam radius results in higher laser intensity that compensates for the loss in SNR that would otherwise be expected when increasing field-of-view.

This concept is important depending on which imaging mode the system is operating in. For example, if our system uses real aperture processing it would be desired to have limited field-of-view; however, if our system operates with synthetic aperture processing, a larger field-of-view is preferred. A depiction of these imaging modes and their relation to the laser beam radius is shown in Fig. 10. In conventional sonar imaging, these two imaging modes are referred to as side-scan sonar and synthetic aperture sonar. We direct the interested reader to [6] and [66] for more

information on applications where each imaging mode is adopted.

V. EXPERIMENTAL RESULTS

The analysis discussed in the previous section has aided the design of a system which can successfully image underwater targets in a fully non-contact manner.

A. EXPERIMENTAL SETUP

The system proof-of-concept has been developed as shown in Fig. 11. Here we use the previously described 71 *kHz* CMUT, though future developed CMUTs with different resonance frequencies could permit a more optimized design that follows the framework depicted in Fig. 8. Whereas our analysis above indicates that the ideal laser wavelength (assuming pure water) for a 71 *kHz* acoustic frequency is around 1250 *nm*, this optical wavelength is not commercially available with relatively high optical power. As a result, we choose to operate with a Ytterbium laser at 1070 *nm* where peak optical powers in the kilo-Watt range are available in fiber laser modules. We determined that the deviation from the optimal wavelength is more than compensated for by the available optical power by using (9).

To couple the optical beam to free space, we use a fiber-terminating collimator. Optical intensity modulation frequencies in the *kHz*-range are not easily achieved directly from laser modules, so we opt for external modulation through the use of an acousto-optic modulator (AOM) [67].

After generation of acoustic waves in water through the photoacoustic effect, the echoes from the targets are received
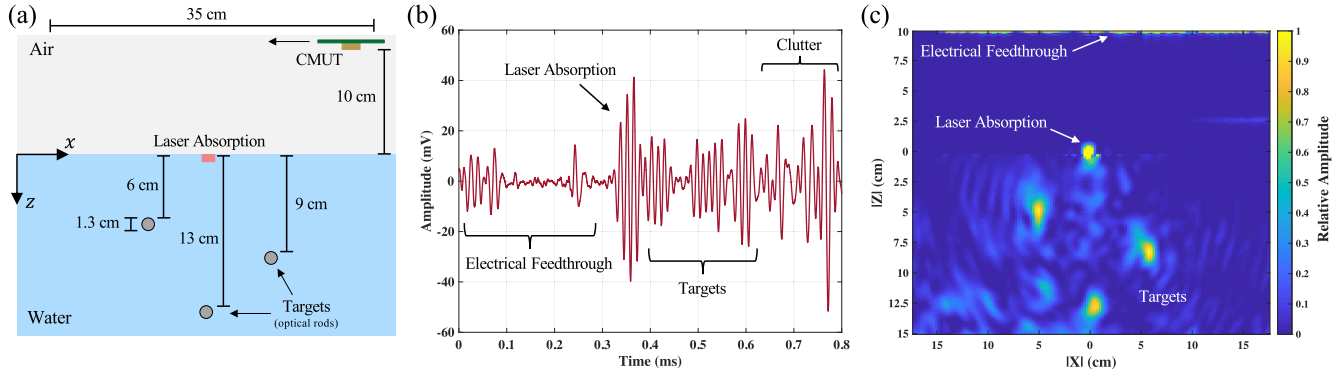
FIGURE 12. (a) Ground truth object distribution, (b) Example CMUT received signal, (c) Reconstructed image of captured measurements using our airborne sonar system.

in air by the CMUT receiver. The CMUT analog front-end electronics convert the changes in capacitance to a voltage signal through a low-noise transimpedance amplifier (LNA) and subsequent voltage amplification stages. The signals are coherently detected as the CMUT is mechanically scanned in the x-direction and are digitized and then fed to the digital signal processing stage. The primary signal processing step is the frequency-domain filtering around the CMUT bandwidth to eliminate out-of-band noise that is introduced by the analog front-end circuits. It is worth noting that the height of the CMUT from the surface of water is chosen to be 10 cm for the proof-of-concept experiments but could be scaled to several meters in more realistic system demonstrations.

B. IMAGE RECONSTRUCTION ALGORITHM
To reconstruct an image with sufficient resolution, we must either implement a large physical array of CMUTs or capture sufficient data through a synthetic aperture. By mechanically scanning the CMUT receiver and ensuring coherent detection, we mimic simultaneous detection with a large physical array of CMUTs, i.e. we implement a synthetic aperture. In our experiments, the extent of this synthetic aperture is 35 cm.

The development of synthetic aperture radar (SAR) image reconstruction algorithms dates back several decades due to the deployment of aerial and satellite imaging systems [68]. The conventional SAR algorithms, however, are intended for image reconstruction in a homogeneous medium and are not effective for our application where the propagation spans both air and water.

More recently, interest in image reconstruction in inhomogeneous media for applications such as through-wall imaging and medical imaging has led to the development of a piece-wise SAR (PW-SAR) algorithm [69] which permits imaging in layered structures – as we have in our application.

For a synthetic aperture in air, we collect the received data which can be denoted as $s(x, z = h, t)$ following the coordinate system noted in Fig. 11. The PW-SAR algorithm migrates this data to the object locations in space through phase migration of plane waves. The plane waves can be decomposed from the received data through Fourier Trans-

forms over both time and the spatial variable x yielding $S(k_x, z = h, f)$ where k_x is the spatial-frequency variable and f is the time-frequency variable. To migrate the plane waves, the PW-SAR imaging equation is used:

$$\Gamma(x', z') = \sum_f F_x^{-1}\{S(k_x, z = h, f) \cdot e^{j(k_{z,a}h + k_{z,w}|z'|)}\}, \quad (10)$$

where $\Gamma(x', z')$ is the reconstructed image, F_x^{-1} represents the inverse spatial Fourier Transform, and $k_{z,i}$ is found through the dispersion relation:

$$k_i^2 = k_{x,i}^2 + k_{z,i}^2, \quad (11)$$

where k_i is the acoustic wavenumber in medium i and $k_{x,i}$ and $k_{z,i}$ are its spatial components in the x and z directions. In (10), $i = a$ refers to the air medium and $i = w$ refers to the water medium. More details on the full implementation of the PW-SAR algorithm can be found in [69].

Here, we must further modify the PW-SAR algorithm to enable image reconstruction for a bistatic imaging geometry; our application is bistatic since the acoustic source exists at the surface of water while the acoustic detection is at the airborne platform. The PW-SAR imaging equation in (10) combined with the dispersion relation in (11) solely accounts for phase accumulation from the object location (x', z') to the receivers. In our system, phase is also accumulated from the point of optical absorption $(x_0, z_0 = 0)$ to the objects. To implement this phase correction, we augment the PW-SAR imaging equation:

$$\Gamma(x', z') = e^{jk_w r}\sum_f F_x^{-1}\{S(k_x, z = h, f) \cdot e^{j(k_{z,a}h + k_{z,w}|z'|)}\},$$
$$(12)$$

where r is the radial distance from the point of optical absorption to the object location and can be defined as:

$$r = \sqrt{(x_0 - x')^2 + (z')^2}. \quad (13)$$

C. IMAGING RESULTS
Using the modified PW-SAR algorithm following a synthetic aperture data capture with the CMUT receiver, we reconstruct the image shown in Fig. 12(c).

In Fig. 12(a), the true distribution of the underwater targets (optical rods) is shown. The optical rods are placed such that they are perpendicular to the CMUT scan direction. The targets and their placement were chosen to reduce the dimensionality of the problem to two-dimensions. Future imaging experiments will perform a two-dimensional CMUT scan which will permit three-dimensional underwater imaging of more complex objects. In addition, the depth of the targets is currently limited by the dimensions of the water tank and is not fundamentally constrained; Fig 12(b) shows that the signals reflected from the targets are received with plenty of SNR despite using only a fraction of the laser's peak power for the experiment.

The reconstructed image in Fig. 12(c) clearly shows the targets positioned at the correct locations. Artifacts in the image are primarily a result of clutter due to multiple reflections off of the water tank walls as well as those that are inherent to narrowband imaging systems. Our future work aims to incorporate multi-frequency CMUTs to improve imaging resolution and suppress the artifacts that arise from image reconstruction with narrowband signals.

Whereas previous works [13], [14] have been limited to collecting one-dimensional signals similarly to those shown in Fig. 12(b), our proof-of-concept system has successfully demonstrated a reconstructed image – allowing for spatial localization of underwater objects.

VI. CONCLUSION

In an imaging scenario where conventional sensing technologies fail, our hybrid optical-acoustic system has successfully demonstrated underwater acoustic imaging in a fully airborne manner for the first time. By exploiting the linear photoacoustic effect, this system capitalizes on the benefits of underwater acoustic propagation and permits high sensitivity acoustic detection in air using low-frequency CMUTs that enable array processing. Unlike optical imaging, the underwater acoustic nature of our system is more robust in turbid waters and at greater depths and has high potential for future scalability and large-scale deployment. In comparison to previous works aiming to design an airborne sonar system [13]–[16], this work goes beyond capturing one-dimensional signals by reconstructing the first image of its kind that allows for localization of embedded underwater objects.

To achieve this, we derive a solution to the photoacoustic wave equation which we use to guide our design within a design space that is not well explored in the literature. The analysis and design framework presented in this paper could also be applied to many other application spaces involving laser-induced acoustic generation at the surface of an optically absorbent medium via the photoacoustic effect. In non-contact non-destructive testing, the laser excitation typically exploits the linear photoacoustic mechanism to prevent damage that would be caused by the ablative or dielectric breakdown mechanisms [70]. In addition, the medical imaging applications must also be in the linear photoacoustic regime to satisfy the ANSI limits for optical exposure [34]. With this

in mind, the analysis herein is particularly valuable especially if non-contact ultrasonic detection with CMUTs is explored for these applications [34]–[37], [70]–[75].

While there are clear advantages of the proposed system over conventional remote sensing techniques, there are many challenges that remain to be addressed. Future work includes investigating the influence of ocean waves on our system's purely ultrasonic detection, scaling to CMUT arrays which may incorporate multiple frequencies for imaging resolution enhancement, and performing larger scale imaging experiments in more realistic environments.

APPENDIX
DERIVATION OF DESIGN EQUATION

The wave equation provided in (3) can be effectively solved in the frequency-domain by first taking the Fourier Transform with respect to time:

$$\left(\nabla^2 + k^2\right) P(\mathbf{r}, \omega) = -\frac{j\omega\beta}{C_p} H(\mathbf{r}, \omega), \tag{14}$$

where k is the acoustic wavenumber, ω is the angular frequency, and the capital letters P and H are used to signify the frequency-domain representation of the pressure and heating function. This equation is referred to as the Inhomogeneous Helmholtz Equation which has the unique solution of the convolution of the source function with the appropriate Green's Function if the Sommerfeld radiation boundary condition is invoked [76]:

$$P(\mathbf{r}, \omega) = \frac{j\omega\beta}{C_p} \int_{IR^3} G(\mathbf{r} - \mathbf{r}')H(\mathbf{r}', \omega)d\mathbf{r}'. \tag{15}$$

Here, the primed variable is used to represent locations within the source distribution or equivalently the region of optical absorption. To effectively capture the reflected wave off the interface, the Green's Function that enforces the free-surface boundary condition is applied [77]:

$$G(\mathbf{r} - \mathbf{r}') = \frac{e^{-jk|\mathbf{r}-\mathbf{r}'|}}{4\pi |\mathbf{r} - \mathbf{r}'|} - \frac{e^{-jk|\mathbf{r}+\mathbf{r}'|}}{4\pi |\mathbf{r} + \mathbf{r}'|}. \tag{16}$$

The first term of the Green's Function in (16) accounts for the downward propagating wave while the second term realizes the reflected wave. The heating function contains all system design parameters and is separable in space and time:

$$H(\mathbf{r}', \omega) = h(\mathbf{r}')H(\omega), \tag{17}$$

where $h(\mathbf{r})$ is the spatial distribution of the optical absorption and $H(\omega)$ is the Fourier Transform of the optical intensity modulation function.

Invoking a far-field assumption results in a solution to the Inhomogeneous Helmholtz Equation that is generally applicable to any heating function:

$$P(\mathbf{r}, \omega) = \frac{j\omega\beta}{C_p} \frac{H(\omega)e^{-jkr}}{4\pi r} \int_{IR^3} h(\mathbf{r}')(e^{jk\mathbf{r}'} - e^{-jk\mathbf{r}'})d\mathbf{r}'. \tag{18}$$

The remaining exponential terms within the integration are the phase compensation terms that account for the forward
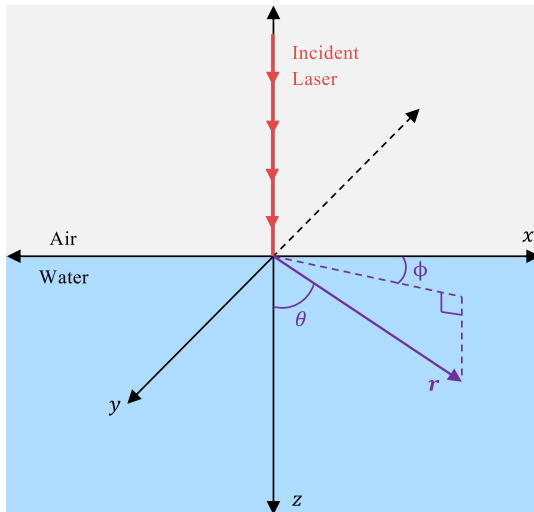
FIGURE 13. Coordinate system assumed in the derivation and solution to the photoacoustic wave equation.

propagating wave and reflected wave. Assuming a Gaussian laser beam with radius a and peak power H_0, the complete frequency-domain solution to the wave equation is [50], [63]:

$$P(\mathbf{r}, \omega) = \frac{-T\omega\beta}{2C_p} \frac{H_0\tilde{H}(\omega)e^{-jkr}}{r} \frac{\mu k cos\theta}{\mu^2 + k^2 cos^2\theta} e^{-k^2a^2 sin^2\theta/4}, \quad (19)$$

where T is the optical transmission coefficient into the water, μ is the optical absorption coefficient, $\tilde{H}(\omega)$ is the normalized optical modulation function, and θ and ϕ are the angles depicted in Fig. 13. Since the laser beam is assumed to be Gaussian, the pressure distribution is cylindrically symmetric, or is constant across ϕ.

ACKNOWLEDGMENT

REFERENCES

[1] J. S. Collier and S. R. Humber, "Time-lapse side-scan sonar imaging of bleached coral reefs: A case study from the seychelles," *Remote Sens. Environ.*, vol. 108, no. 4, pp. 339–356, Jun. 2007.

[2] W. I. Stewart, D. Chu, S. Malik, S. Lerner, and H. Singh, "Quantitative seafloor characterization using a bathymetric sidescan sonar," *IEEE J. Ocean. Eng.*, vol. 19, no. 4, pp. 599–610, 1994.

[3] P. K. LeHardy and J. Larsen, "Deepwater synthetic aperture sonar and the search for MH370," in *Proc. OCEANS MTS/IEEE Washington*, Oct. 2015, pp. 1–4.

[4] G. J. Dobeck, "Fusing sonar images for mine detection and classification," *Proc. SPIE*, vol. 3710, Aug. 1999, pp. 602–614.

[5] M. P. Hayes and P. T. Gough, "Synthetic aperture sonar: A review of current status," *IEEE J. Ocean. Eng.*, vol. 34, no. 3, pp. 207–224, Jul. 2009.

[6] P. Blondel, *The Handbook of Sidescan Sonar*. Chichester, U.K.: Springer, 2010.

[7] T. Meissner and F. J. Wentz, "The complex dielectric constant of pure and sea water from microwave satellite observations," *IEEE Trans. Geosci. Remote Sens.*, vol. 42, no. 9, pp. 1836–1849, Sep. 2004.

[8] G. Benelli, A. Pozzebon, and M. Reaz, *RFID Under Water: Technical Issues and Applications*. Rijeka, Croatia: InTech, 2013.

[9] A. Pozzebon, "Bringing near field communication under water: Short range data exchange in fresh and salt water," in *Proc. Int. EURASIP Workshop RFID Technol. (EURFID)*, Oct. 2015, pp. 152–156.

[10] G. M. Hale and M. R. Querry, "Optical constants of water in the 200-nm to 200-μm wavelength region," *Appl. Opt.*, vol. 12, no. 3, pp. 555–563, 1973.

[11] B. Wozniak and J. Dera, *Light Absorption Sea Water*, vol. 33. New York, NY, USA: Springer, 2007.

[12] M. Babin, A. Morel, V. Fournier-Sicre, F. Fell, and D. Stramski, "Light scattering properties of marine particles in coastal and open ocean waters as related to the particle mass concentration," *Limnology Oceanogr.*, vol. 48, no. 2, pp. 843–859, Mar. 2003.

[13] D. Farrant, J. Burke, L. Dickinson, P. Fairman, and J. Wendoloski, "Opto-acoustic underwater remote sensing (OAURS)—An optical sonar?" in *Proc. Oceans IEEE Sydney*, May 2010, pp. 1–7.

[14] L. Antonelli and F. Blackmon, "Experimental demonstration of remote, passive acousto-optic sensing," *J. Acoust. Soc. Amer.*, vol. 116, no. 6, pp. 3393–3403, Dec. 2004.

[15] F. Blackmon and L. Antonelli, "Remote, aerial, opto-acoustic communications and sonar," *Proc. SPIE*, vol. 5778, pp. 800–808, May 2005.

[16] F. A. Blackmon and L. T. Antonelli, "Experimental detection and reception performance for uplink underwater acoustic communication using a remote, in-air, acousto-optic sensor," *IEEE J. Ocean. Eng.*, vol. 31, no. 1, pp. 179–187, Jan. 2006.

[17] B. Ma, K. Firouzi, K. Brenner, and B. T. Khuri-Yakub, "High sensitivity and wide bandwidth airborne CMUTs with low driving voltage," in *Proc. IEEE Int. Ultrason. Symp. (IUS)*, Oct. 2019, pp. 1201–1204.

[18] O. Oralkan, A. S. Ergun, C.-H. Cheng, J. A. Johnson, M. Karaman, T. H. Lee, and B. T. Khuri-Yakub, "Volumetric ultrasound imaging using 2-D CMUT arrays," *IEEE Trans. Ultrason., Ferroelectr., Freq. Control*, vol. 50, no. 11, pp. 1581–1594, Nov. 2003.

[19] A. Singhvi, K. C. Boyle, M. Fallahpour, B. T. Khuri-Yakub, and A. Arbabian, "A microwave-induced thermoacoustic imaging system with non-contact ultrasound detection," *IEEE Trans. Ultrason., Ferroelectr., Freq. Control*, vol. 66, no. 10, pp. 1587–1599, Oct. 2019.

[20] P. Filippi, A. Bergassoli, D. Habault, and J. P. Lefebvre, *Coustics: Basic Physics, Theory, and Methods*. Amsterdam, The Netherlands: Elsevier, 1998.

[21] C. L. Morfey, *Dictionary of Acoustics*. New York, NY, USA: Academic, 2000.

[22] H. Singh, "Submarine communications," *Defence Sci. J.*, vol. 43, no. 1, p. 43, 1993.

[23] C. A. Balanis, *Antenna Theory: Analysis and Design*. Hoboken, NJ, USA: Wiley, 2016.

[24] L. Bartolini, L. De Dominicis, M. F. de Collibus, G. Fornetti, M. Guarneri, E. Paglia, C. Poggi, and R. Ricci, "Underwater three-dimensional imaging with an amplitude-modulated laser radar at a 405 nm wavelength," *Appl. Opt.*, vol. 44, no. 33, pp. 7130–7135, 2005.

[25] J. Busck, "Underwater 3-D optical imaging with a gated viewing laser radar," *Opt. Eng.*, vol. 44, no. 11, Nov. 2005, Art. no. 116001.

[26] H. M. Tulldahl and M. Pettersson, "Lidar for shallow underwater target detection," *Proc. SPIE*, vol. 6739, Nov. 2007, Art. no. 673906.

[27] J. W. McLean and J. D. Freeman, "Effects of ocean waves on airborne lidar imaging," *Appl. Opt.*, vol. 35, no. 18, pp. 3261–3269, 1996.

[28] J. W. McLean, "High-resolution 3D underwater imaging," *Proc. SPIE*, vol. 3761, pp. 10–19, Oct. 1999.

[29] J. H. Churnside and J. J. Wilson, "Airborne lidar imaging of salmon," *Appl. Opt.*, vol. 43, no. 6, pp. 1416–1424, 2004.

[30] F. Pellen, P. Olivard, Y. Guern, J. Cariou, and J. Lotrian, "Radio frequency modulation on an optical carrier for target detection enhancement in sea-water," *J. Phys. D, Appl. Phys.*, vol. 34, no. 7, p. 1122, 2001.

[31] J. Shang, Y. Liu, J. Sun, D. W. Kim, W. Chen, and Y. He, "Five-channel fiber-based laser Doppler vibrometer for underwater acoustic field measurement," *Appl. Opt.*, vol. 59, no. 3, pp. 676–682, 2020.

[32] G. Wissmeyer, M. A. Pleitez, A. Rosenthal, and V. Ntziachristos, "Looking at sound: Optoacoustics with all-optical ultrasound detection," *Light: Sci. Appl.*, vol. 7, no. 1, pp. 1–16, Dec. 2018.

[33] E. Zhang, J. Laufer, and P. Beard, "Backward-mode multiwavelength photoacoustic scanner using a planar fabry-perot polymer film ultrasound sensor for high-resolution three-dimensional imaging of biological tissues," *Appl. Opt.*, vol. 47, no. 4, pp. 561–577, 2008.

[34] X. Zhang, J. R. Fincke, C. M. Wynn, M. R. Johnson, R. W. Haupt, and B. W. Anthony, "Full noncontact laser ultrasound: First human data," *Light, Sci. Appl.*, vol. 8, no. 1, pp. 1–11, Dec. 2019.

[35] A. Hochreiner, J. Bauer-Marschallinger, P. Burgholzer, B. Jakoby, and T. Berer, "Non-contact photoacoustic imaging using a fiber based interferometer with optical amplification," *Biomed. Opt. Express*, vol. 4, no. 11, pp. 2322–2331, 2013.

[36] Y. Wang, C. Li, and R. K. Wang, "Noncontact photoacoustic imaging achieved by using a low-coherence interferometer as the acoustic detector," *Opt. Lett.*, vol. 36, no. 20, pp. 3975–3977, 2011.

[37] G. Rousseau, A. Blouin, and J.-P. Monchalin, "Non-contact photoacoustic tomography and ultrasonography for tissue imaging," *Biomed. Opt. Express*, vol. 3, no. 1, pp. 16–25, 2012.

[38] Y. Fu, M. Guo, and P. B. Phua, "Spatially encoded multibeam laser Doppler vibrometry using a single photodetector," *Opt. Lett.*, vol. 35, no. 9, pp. 1356–1358, 2010.

[39] V. Aranchuk, A. K. Lal, C. F. Hess, and J. M. Sabatier, "Multi-beam laser Doppler vibrometer for landmine detection," *Opt. Eng.*, vol. 45, no. 10, Oct. 2006, Art. no. 104302.

[40] E. Cupido, S. Morel, and D. Smith, "Multipoint laser Doppler vibrometer for transient analysis," *Proc. IMAC XXI*, 2003, pp. 651–656.

[41] J. Kilpatrick and V. Markov, "Multi-pixel (matrix) laser vibrometer," in *Applications of Lasers for Sensing and Free Space Communications*, 2010, Art. no. LSWA3.

[42] L. V. Wang, *Photoacoustic Imaging and Spectroscopy*. Boca Raton, FL, USA: CRC Press, 2017.

[43] L. M. Lyamshev, "Optoacoustic sources of sound," *Sov. Phys. Uspekhi*, vol. 24, no. 12, p. 977, 1981.

[44] H. K. Park, D. Kim, C. P. Grigoropoulos, and A. C. Tam, "Pressure generation and measurement in the rapid vaporization of water on a pulsed-laser-heated surface," *J. Appl. Phys.*, vol. 80, no. 7, pp. 4072–4081, Oct. 1996.

[45] N. P. Chotiros, "Nonlinear optoacoustic underwater sound source," *Proc. SPIE*, vol. 925, pp. 255–262, Aug. 1988.

[46] C. G. A. Hoelen and F. F. M. de Mul, "A new theoretical approach to photoacoustic signal generation," *J. Acoust. Soc. Amer.*, vol. 106, no. 2, pp. 695–706, Aug. 1999.

[47] D. Devaux, R. Fabbro, L. Tollier, and E. Bartnicki, "Generation of shock waves by laser-induced plasma in confined geometry," *J. Appl. Phys.*, vol. 74, no. 4, pp. 2268–2273, Aug. 1993.

[48] C. Sacchi, "Laser-induced electric breakdown in water," *J. Opt. Soc. Amer. B, Opt. Phys.*, vol. 8, no. 2, pp. 337–345, 1991.

[49] A. Vogel, S. Busch, and U. Parlitz, "Shock wave emission and cavitation bubble generation by picosecond and nanosecond optical breakdown in water," *J. Acoust. Soc. Amer.*, vol. 100, no. 1, pp. 148–165, Jul. 1996.

[50] F. Blackmon, L. Estes, and G. Fain, "Linear optoacoustic underwater communication," *Appl. Opt.*, vol. 44, no. 18, pp. 3833–3845, Jun. 2005.

[51] F. A. McDonald and G. C. Wetsel, Jr, "Generalized theory of the photoacoustic effect," *J. Appl. Phys.*, vol. 49, no. 4, pp. 2313–2322, 1978.

[52] F. A. McDonald, "Photoacoustic effect and the physics of waves," *Amer. J. Phys.*, vol. 48, no. 1, pp. 41–47, Jan. 1980.

[53] N. P. Chotiros, "The moving thermoacoustic array: A theoretical study," *J. Acoust. Soc. Amer.*, vol. 83, no. 6, pp. 2145–2158, Jun. 1988.

[54] T. L. Szabo, *Diagnostic Ultrasound Imaging: Inside Out*. New York, NY, USA: Academic, 2004.

[55] M. Xu and L. V. Wang, "Photoacoustic imaging in biomedicine," *Rev. Sci. Instrum.*, vol. 77, no. 4, Apr. 2006, Art. no. 041101.

[56] B. Ma, K. Firouzi, K. Brenner, and B. T. Khuri-Yakub, "Wide bandwidth and low driving voltage vented CMUTs for airborne applications," *IEEE Trans. Ultrason., Ferroelectr., Freq. Control*, vol. 66, no. 11, pp. 1777–1785, Nov. 2019.

[57] K. K. Park and B. T. Khuri-Yakub, "3-D airborne ultrasound synthetic aperture imaging based on capacitive micromachined ultrasonic transducers," *Ultrasonics*, vol. 53, no. 7, pp. 1355–1362, Sep. 2013.

[58] K. Brenner, A. Ergun, K. Firouzi, M. Rasmussen, Q. Stedman, and B. Khuri–Yakub, "Advances in capacitive micromachined ultrasonic transducers," *Micromachines*, vol. 10, no. 2, p. 152, Feb. 2019.

[59] H. Nan, K. C. Boyle, N. Apte, M. S. Aliroteh, A. Bhuyan, A. Nikoozadeh, B. T. Khuri-Yakub, and A. Arbabian, "Non-contact thermoacoustic detection of embedded targets using airborne-capacitive micromachined ultrasonic transducers," *Appl. Phys. Lett.*, vol. 106, no. 8, Feb. 2015, Art. no. 084101.

[60] K. C. Boyle, H. Nan, A. Arbabian, and B. T. Khuri-Yakub, "Noncontact thermoacoustic detection of targets embedded in dispersive media," *Proc. SPIE*, vol. 9988, pp. 99880H-1–99880H-7, Oct. 2016.

[61] H. E. Bass, L. C. Sutherland, A. J. Zuckerwar, D. T. Blackstock, and D. M. Hester, "Atmospheric absorption of sound: Further developments," *J. Acoust. Soc. Amer.*, vol. 97, no. 1, pp. 680–683, Jan. 1995.

[62] M. Cheney and B. Borden, *Fundamentals of Radar Imaging*. Philadelphia, PA, USA: SIAM, 2009.

[63] L. Lyamshev, "Radiation acoustics," *Le J. de Phys. Colloques*, vol. 51, no. C2, pp. 1–2, 1990.

[64] J. A. Curcio and C. C. Perry, "The near infrared absorption spectrum of liquid water," *J. Opt. Soc. Amer. A, Opt. Image Sci.*, vol. 41, no. 5, pp. 302–304, May 1951.

[65] R. E. Francois and G. R. Garrison, "Sound absorption based on ocean measurements. Part II: Boric acid contribution and equation for total absorption," *J. Acoust. Soc. Amer.*, vol. 72, no. 6, pp. 1879–1890, Dec. 1982.

[66] R. E. Hansen and N. Kolev, *Introduction to Synthetic Aperture Sonar*. London, U.K.: INTECH Open Access Publisher, 2011.

[67] N. A. Riza, *Photonic Signals Systems: An Introduction*. New York, NY, USA: McGraw-Hill, 2013.

[68] J. C. Kirk, "A discussion of digital processing in synthetic aperture radar," *IEEE Trans. Aerosp. Electron. Syst.*, vol. AES-11, no. 3, pp. 326–337, May 1975.

[69] M. Fallahpour, J. T. Case, M. T. Ghasr, and R. Zoughi, "Piecewise and Wiener filter-based SAR techniques for monostatic microwave imaging of layered structures," *IEEE Trans. Antennas Propag.*, vol. 62, no. 1, pp. 282–294, Jan. 2014.

[70] S.-T. Luo, X.-L. Tan, M.-C. Pan, and C.-G. Fan, "Progress of laser-generated ultrasonic non-destructive testing technology," *Proc. SPIE*, vol. 8192, Aug. 2011, Art. no. 81924C.

[71] X. L. Deán-Ben, G. A. Pang, F. Montero de Espinosa, and D. Razansky, "Non-contact optoacoustic imaging with focused air-coupled transducers," *Appl. Phys. Lett.*, vol. 107, no. 5, Aug. 2015, Art. no. 051105.

[72] S. Everton, P. Dickens, C. Tuck, and B. Dutton, "Evaluation of laser ultrasonic testing for inspection of metal additive manufacturing," *Proc. SPIE*, vol. 9353, Mar. 2015, Art. no. 935316.

[73] K.-T. Wu, C.-K. Jen, M. Kobayashi, and A. Blouin, "Integrated piezoelectric ultrasonic receivers for laser ultrasound in non-destructive testing of metals," *J. Nondestruct. Eval.*, vol. 30, no. 1, pp. 1–8, Mar. 2011.

[74] I. Pelivanov, T. Buma, J. Xia, C.-W. Wei, and M. O'Donnell, "A new fiber-optic non-contact compact laser-ultrasound scanner for fast non-destructive testing and evaluation of aircraft composites," *J. Appl. Phys.*, vol. 115, no. 11, Mar. 2014, Art. no. 113105.

[75] Y. Zhao, J. Chen, J. Sun, J. Song, J. Ma, S. Liu, and Y. Zhu, "Applications of laser ultrasonic technique on nondestructive testing and evaluation of materials," in *MATEC Web Conferences*, vol. 173. Les Ulis, France: EDP Sciences, 2018, p. 02033.

[76] A. Sommerfeld, *Partial Differential Equations in Physics*. New York, NY, USA: Academic, 1949.

[77] A. Bozhkov and F. V. Bunkin, "Generation of sound in a liquid as a result of absorption of modulated laser radiation," *Sov. J. Quantum Electron.*, vol. 5, no. 8, p. 956, 1975.

AIDAN FITZPATRICK (Graduate Student Member, IEEE) received the B.S. degree in electrical and computer engineering from the University of Massachusetts Amherst, in 2018, and the M.S. degree in electrical engineering from Stanford University in 2020, where he is currently pursuing the Ph.D. degree in electrical engineering.

In 2017, he interned with MACOM Technology Solutions on their device modeling and research and development team working on power amplifier design and testing. In 2018, he performed research on antenna design and RF system design at the University of Massachusetts Amherst. His current research interests lie at the intersection of electromagnetics, acoustics, and signal processing for imaging algorithm development and system design for non-contact thermoacoustic/photoacoustic, and millimeter wave applications.

AJAY SINGHVI (Member, IEEE) received the B.E. degree in electrical and electronics engineering from Birla Institute of Technology and Science (BITS) Pilani, India, in 2015. He is currently pursuing the joint M.S. and Ph.D. degree in electrical engineering from Stanford University.

From 2014 to 2015, he worked with Prof. P. Beerel at the University of Southern California, where his research was aimed at building low power asynchronous circuits. In 2018, he was with Kilby Labs, Texas Instruments, Santa Clara, CA, USA, where he designed front-end architectures and circuits for lidar systems. His current research interests include design of integrated circuit systems and algorithms for non-contact thermoacoustic/photoacoustic and ultrasound imaging, sensing, and communication applications.

Mr. Singhvi was a recipient of the L. K. Maheshwari Best Graduating Student Award from BITS Pilani in 2014 and the Analog Devices Outstanding Student Designer Award in 2020.

AMIN ARBABIAN (Senior Member, IEEE) received the Ph.D. degree in electrical engineering and computer science from the University of California at Berkeley, Berkeley, CA, USA, in 2011.

From 2007 to 2008, he was a part of the Initial Engineering Team, Tagarray, Inc., Palo Alto, CA, USA (now acquired by Maxim Integrated Inc.). In 2010, he joined Qualcomm's Corporate Research and Development Division, San Diego, CA, USA, where he designed circuits for next-generation ultralow power wireless transceivers. In 2012, he joined Stanford University, Stanford, CA, USA, where he is currently an Associate Professor of electrical engineering. His current research interests include mm-wave and high-frequency circuits and systems, imaging technologies, Internet-of-Everything devices, including wireless power delivery techniques, and medical implants. He was a recipient or co-recipient of the 2020 IEEE Transactions on Biomedical Circuits and Systems Best Paper Award, the 2016 Stanford University Tau Beta Pi Award for Excellence in Undergraduate Teaching, the 2015 NSF CAREER Award, the 2014 DARPA Young Faculty Award, including the Director's Fellowship in 2016, the 2013 Hellman Faculty Scholarship, the 2010–2011, 2014–2015, and 2016–2017 Qualcomm Innovation Fellowships, and best paper awards at the 2017 IEEE Biomedical Circuits and Systems Conference, the 2016 IEEE Conference on Biomedical Wireless Technologies, Networks, and Sensing Systems, the 2014 IEEE VLSI Circuits Symposium, the 2013 IEEE International Conference on Ultra-Wideband, the 2010 IEEE Jack Kilby Award for Outstanding Student Paper at the International SolidState Circuits Conference, and two-time second place best student paper awards at 2008 and 2011 RFIC Symposiums. He currently serves on the steering committee for RFIC Symposium, the technical program committees of RFIC Symposium and VLSI Circuits Symposium, and as an Associate Editor for IEEE Solid-State Circuits Letters and the IEEE Journal of Electromagnetics, RF, and Microwaves in Medicine and Biology.

• • •